

## Full Length Article

# Accelerating and stabilizing the vapor-liquid equilibrium (VLE) calculation in compositional simulation of unconventional reservoirs using deep learning based flash calculation



Shihao Wang<sup>a,\*</sup>, Nicolas Sobecki<sup>b</sup>, Didier Ding<sup>b</sup>, Lingchen Zhu<sup>c</sup>, Yu-Shu Wu<sup>a</sup>

<sup>a</sup> Petroleum Engineering Department, Colorado School of Mines, Golden, CO 80401, USA

<sup>b</sup> IFPEN, France

<sup>c</sup> Schlumberger Doll Research Center, Cambridge, MA 02139, USA

## ARTICLE INFO

## Keywords:

Flash calculation  
Unconventional reservoirs  
Deep learning  
Proxy calculation  
Reservoir simulation

## ABSTRACT

The flash calculation with large capillary pressure often turns out to be time-consuming and unstable. Consequently, the compositional simulation of unconventional oil/gas reservoirs, where large capillary pressure exists on the vapor-liquid phase interface due to the narrow pore channel, becomes a challenge to traditional reservoir simulation techniques. In this work, we try to resolve this issue by combining deep learning technology with reservoir simulation. We have developed a compositional simulator that is accelerated and stabilized by stochastically-trained proxy flash calculation.

We first randomly generated 300,000 data samples from a standalone physical flash calculator. We have constructed a two-step neural network, in which the first step is the classify the phase condition of the system and the second step is to predict the concentration distribution among the determined phases. Each network consists of four hidden layers in between the input layer and the output layer. The network is trained by Stochastic Gradient Descent (SGD) method with 100 epochs.

With given temperature, pressure, feed concentration pore radius, the trained network predicts the phases and concentration distribution in the system with very low computational cost. Our results show that the accuracy of the network is above 97% in the metric of mean absolute percentage error. The predicted result is used as the initial guess of the flash calculation module in the reservoir simulator. With the implementation of the deep learning based flash calculation module, the speed of the simulator has been effectively increased and the stability (in the manner of the ratio of convergence) has been improved as well.

## 1. Introduction

The oil and gas stored in unconventional reservoirs has some unique transport mechanism and phase behavior, including the pore confine effect [1,2], the large capillary pressure effect [3,4], multiscale pore structures [5] and gas slippage effect [6–9]. Moreover, the prediction of the complex phase behaviors in unconventional reservoirs requires compositional modeling, of which the flash calculation is an essential yet time-consuming portion. To improve the speed as well as the stability of the flash calculation, several techniques have been adopted, including reduction method [10], phase stability test [11] and so on. Recently, the fast-arising artificial intelligence (AI) techniques have drawn the attention of researchers. Particularly, the fast development of the optimization algorithm, as well as hardware infrastructure, have greatly promoted the advance of stochastic learning techniques. The

rapid development of GPU enables the training of deep learning (DL) networks (also known as Artificial Neural Network (ANN)) [12]. There are several trials of combining AI with flash calculation. Gaganis et al. [13,14] are among the first to propose the application of neural network approach in developing proxy flash calculation. In their work, support vector classifier (SVC) is used to conduct phase stability test and a single layer ANN network is used to replace the physical flash calculation for liquid-vapor phase equilibrium calculation. Kashinath et al. [15] further improved Gaganis et al.'s model by bringing out a novel framework to conduct an isothermal flash calculation. In their work, the relevance vector machine [16] is combined with a single-layer artificial neural network. The former technique is used to classify phase condition, while the latter is used to determine the concentration distribution. All these proxy models have shown sound accuracy and have been successfully implemented into reservoir simulators,

\* Corresponding author.

E-mail address: [shiwang@mines.edu](mailto:shiwang@mines.edu) (S. Wang).

<https://doi.org/10.1016/j.fuel.2019.05.023>

Received 12 March 2019; Received in revised form 3 May 2019; Accepted 4 May 2019

Available online 09 May 2019

0016-2361/ © 2019 Elsevier Ltd. All rights reserved.

improving the speed of compositional simulation. Moreover, El-Sebakhy [17] and Rafiee-Taghanaki et al. [18] used the support vector machine technique [19–22] to predict the PVT properties of crude oil, including gas oil ratio, oil volume factor, density and so on. Artificial neural networks have also been used to predict the PVT behavior of crude oil [23] and gas mixtures [24]. Nikraves et al. [25] reviewed the applications of artificial intelligence techniques in the exploration and development of petroleum reservoirs.

In this work, we further extend the work listed above to the compositional simulation of unconventional reservoirs with large capillary pressure effect. We have developed a deep-learning based flash calculation module (proxy flash calculation) for the prediction of phase behaviors of oil and gas in unconventional reservoirs. This proxy flash calculation adopts multi-layer fully connected layers to regress the training data. The input parameters of our model include pressure, temperature, feed concentration and pore radius. The accuracy of the network is above 97% in the metric of mean absolute percentage error. The proxy flash calculation module is used as a preconditioner of the physical flash calculation and has been implemented in a reservoir simulator. We have also compared the performance of the network with different number of hidden layers. The novelty of this work lies in the implementation of the deep learning based flash calculation module as a preconditioner for both phase condition detection and concentration determination, which improves the speed as well as the stability of compositional simulation of unconventional reservoirs while maintaining the same results as physical flash calculation.

This paper is organized as follows. In Chapter 2, we present the physical flash calculation used to train the network. In Chapter 3, we describe the structure, training as well as results of our deep-learning based flash calculation module. In Chapter 4, we describe the implementation of the developed module into an in-house reservoir simulator. In Chapter 5, we present the results of field scale reservoir simulation. In Chapter 6, we summarize and conclude this work.

## 2. Forward modeling

In this section, we briefly introduce the governing equations and flash calculation module used for the forward modeling.

### 2.1. Flow governing equations

The reservoir simulator used in this work is named as MSFLOW\_CO2 [3,26,27]. MSFLOW\_CO2 is a general three-dimensional reservoir simulator for the simulation of complex multiphase flow in porous media. Based on the law of mass conservation, the flow governing equations of MSFLOW\_CO2 describe the transport of hydrocarbon components in a petroleum reservoir. For a vapor-liquid compositional system with  $N_C$  components, the mass conservation equation for component  $k$  is as below

$$\frac{\partial}{\partial t} \left( \phi \sum_{\beta} S_{\beta} \rho_{\beta} x_{\beta}^k \right) = \nabla \cdot \left[ -K_a \frac{K_{r\beta} \rho_{\beta}}{\mu_{\beta}} (\nabla P_{\beta} - \rho_{\beta} \vec{g}) x_{\beta}^k \right] + q^k, \dots, \beta = L, G, \dots, k = 1, \dots, N_C \quad (1)$$

where  $\phi$  is the rock porosity.  $\beta$  is the phase index referring to the liquid (L) or vapor/gas (G) phase.  $S_{\beta}$  and  $\rho_{\beta}$  are the saturation and density of phase  $\beta$ , respectively.  $K_{r\beta}$ ,  $\mu_{\beta}$  and  $P_{\beta}$  are the relative permeability, viscosity and pressure of phase  $\beta$ , respectively.  $K_a$  is the apparent permeability. While for the liquid phase,  $K_a$  is the same as the rock absolute permeability  $K_{\infty}$ , for the vapor phase,  $K_a = K_{\infty}(1 + b/p)$ , in which  $b$  is the Klinkenberg parameter is  $x_{\beta}^k$  the mole concentration of component  $k$  in phase  $\beta$ .  $\vec{g}$  is the gravity term and  $q$  is the sink/source term. In this work the pore compressibility is temporally ignored.

In MSFLOW\_CO2, Eq. (1) is discretized and solved by the Integrated Finite Difference (IFD) method, the details of which can be found in Ref.

[28]. The flow between the rock matrix and the fracture system is described by the dual-porosity model [29]. The nonlinear system resulted from the discretization of IFD is solved by Newton-Raphson's approach. Within each nonlinear iteration, the resulted linear system is solved by a multiscale linear solver [30].

### 2.2. Flash calculation with capillary pressure

In a compositional reservoir simulator, given the pressure ( $P$ ), temperature ( $T$ ) and mole concentration of each component ( $z_i$ ), the flash calculation module predicts the phase condition as well as the concentration of each component in each phase.

In this work, we consider a two-phase system with vapor (V) and liquid (L) phase. The mole concentration of a component in the vapor (gas) phase and in the oil (liquid) phase is denoted respectively as  $y_i$  and  $x_i$ . Meanwhile, the total mole concentration of the vapor phase and the oil phase is denoted as  $n_V$  and  $n_L$  respectively. We then have the following relationship.

$$z_i = x_i n_L + y_i n_V \quad (2)$$

The phase behavior of fluids stored in unconventional reservoirs is unlike that in conventional reservoirs. In the narrow pores of unconventional reservoirs, the capillary pressure  $P_c$  between phases can be no longer ignored [31,32]. For simplicity, in this work, the capillary pressure, which is the difference between the vapor pressure  $p^V$  and the oil phase pressure  $p^L$ , is calculated as below, assuming the oil phase is the wetting phase.

$$P_c = p^V - p^L = \frac{2\sigma_{VL} \cos \theta}{r} \quad (3)$$

In the above equation,  $\sigma_{VL}$  is the interfacial tension between the vapor phase and the liquid phase.  $\theta$  is the contact angle and  $r$  is the pore radius.

$\sigma_{VL}$  is calculated using the model from the work of Macleod [33] and Sugden [34], as follows

$$\sigma_{VL} = (P_a^L \rho^L - P_a^V \rho^V)^v = \left( \rho^L \sum_{i=1}^{N_C} x_i P_{a,i} - \rho^V \sum_{i=1}^{N_C} y_i P_{a,i} \right)^v \quad (4)$$

where  $\rho^L$  and  $\rho^V$  is the molar density of the liquid phase and the vapor phase respectively.  $P_a^L$  and  $P_a^V$  is the parachor for the liquid phase and the vapor phase respectively.  $P_{a,i}$  is the parachor of component  $i$ , the value of which is listed in Table A.2.  $v$  is a parameter that is by default set to be 3.6 [35].

At the equilibrium condition, the fugacity of component  $i$  in the vapor phase  $f_i^v$  and in the liquid phase  $f_i^l$  should be equal, as

$$f_i^v = f_i^l$$

We introduce the fugacity coefficient of component  $i$  in the vapor phase and the liquid phase, as

$$\Phi_i^V = \frac{f_i^V}{y_i p^V} \quad (6)$$

$$\Phi_i^L = \frac{f_i^L}{x_i p^L} \quad (7)$$

Moreover, the equilibrium ratio is defined as

$$K_i = \frac{y_i}{x_i} = \frac{f_i^V / (\Phi_i^V p^V)}{f_i^L / (\Phi_i^L p^L)} = \frac{\Phi_i^L p^L}{\Phi_i^V (p^L + P_c)} \quad (8)$$

By combining Eqs. (5) and (8) and considering the constraints that  $\sum_{i=1}^{N_C} z_i = \sum_{i=1}^{N_C} y_i = \sum_{i=1}^{N_C} x_i = 1$ , we can derive the Rachford-Rice equation as

$$\sum_{i=1}^{N_C} \frac{z_i (K_i - 1)}{n_L + K_i (1 - n_L)} = 0 \quad (9)$$

In this work, Peng-Robin equation of state (PR-EOS) [36] without volume factor correction is used for the calculation of the PVT properties of oil and gas. PR-EOS is a widely adopted cubic equation of state. For phase  $\beta$  (vapor or liquid), the compressibility can be formulated as

$$(Z^\beta)^3 + (B^\beta - 1)(Z^\beta)^2 + (A^\beta - 3(B^\beta)^2 - 2B^\beta)Z^\beta - (A^\beta B^\beta - (B^\beta)^2 - (B^\beta)^3) = 0. \dots \beta = L, V \quad (10)$$

where the term  $A^\beta$  and  $B^\beta$  are defined as follows

$$A^\beta = \frac{a_m p^\beta}{R^2 T^2} \quad (11)$$

$$B^\beta = \frac{b_m p^\beta}{RT} \quad (12)$$

In the above equations,  $Z^\beta$  is the compressibility of phase  $\beta$ . the terms  $a_m$  and  $b_m$  are defined as follows as

$$a_m = \sum_{i=1}^{N_C} \sum_{j=1}^{N_C} z_i z_j a_{ij} \quad (13)$$

$$a_{ij} = (1 - k_{ij}) \sqrt{\alpha_i \alpha_j \alpha_i \alpha_j} \quad (14)$$

$$\alpha_i = 0.45724 \frac{R^2 T_{Ci}^2}{P_{Ci}} \quad (15)$$

$$\alpha_i = [1 + S_i^* (1 - \sqrt{T_{Ci}/T})]^2 \quad (16)$$

$$S_i^* = 0.37464 + 1.54226\omega_i - 0.26992\omega_i^2 \quad (17)$$

$$b_m = \sum_{i=1}^{N_C} b_i \quad (18)$$

$$b_i = 0.0778 \frac{RT_{Ci}}{P_{Ci}} \quad (19)$$

where  $R$  is the gas constant.  $\omega$  is the acentric factor.  $k_{ij}$  is the binary interaction coefficient between component  $i$  and the component  $j$ .  $T_C$  and  $P_C$  is the critical temperature and critical pressure respectively. The critical properties for the hydrocarbon used in this work are from NIST data [37]. The largest root of the cubic equation is assigned to the compressibility of the vapor phase, while the smallest root is assigned to the compressibility of the liquid phase. Based on the assumption of isothermal flash calculation, in PR-EOS, the fugacity coefficients are calculated as

$$\ln(\Phi_i^\beta) = \frac{b_i(Z^\beta - 1)}{b_m} - \ln(Z^\beta - B^\beta) - \frac{A^\beta}{2\sqrt{2}B^\beta} \left( \frac{2\Psi_i}{a_m} - \frac{b_i}{b_m} \right) \ln \left( \frac{Z^\beta + (1 + \sqrt{2})B^\beta}{Z^\beta - (1 - \sqrt{2})B^\beta} \right) \quad (20)$$

In the above equation, the term  $\Psi_i$  is

$$\Psi_i = \sum_j x_j \sqrt{\alpha_i \alpha_j \alpha_i \alpha_j} (1 - k_{ij}) \quad (21)$$

The initial guess of the equilibrium ratio  $K_i^0$  is calculated by Wilson's equation

$$K_i^0 = \frac{P_{ci}}{p} \exp \left( 5.37(1 + \omega_i) \left( 1 - \frac{T_{ci}}{T} \right) \right) \quad (22)$$

Initially, the capillary pressure is set to be 0.

Prior to the flash calculation, a Gibbs energy based phase stability test is performed to preliminarily determine the single phase region. The approach used here follows the work of Sherafati and Jessen [35]. The tangent plane distance (TPD) based on Michelsen's formulation [38] is as follows

$$TPD(\mathbf{z}_T) = \sum_{i=1}^{N_C} z_{Ti} [\mu_i^T(\mathbf{z}_T, P^T) - \mu_i^z(\mathbf{z}, P^z)] \quad (23)$$

where  $\mathbf{z}$  and  $\mathbf{z}_T$  refers to the mole concentration of the feed and a trial phase, respectively.  $\mu_i^T$  and  $\mu_i^z$  is the fugacity of component  $i$  in the trial phase and the feed respectively.  $P^T$  and  $P^z$  is the trial phase pressure and the reference pressure respectively. By switching the variable  $\ln Z_i^T = \ln z_i^T - k$  where  $k$  is the reduced value of the tangent plane distance at the stationary points of Eq. (23), the above equation can be expressed as

$$TPD(\mathbf{Z}_T) = 1 + \sum_{i=1}^{N_C} Z_{Ti} [\ln Z_{Ti} + \ln \varphi_i^T + \ln P^T - (\ln z_i + \ln \varphi_i + \ln P^z) - 1] \quad (24)$$

where  $\varphi_i$  and  $\varphi_i^T$  denotes the fugacity coefficient of component  $i$  in the feed and the trial phase, respectively. Finding the stationary points of TPD is equivalent to solving the below equation

$$\ln Z_{Ti} + \ln \varphi_i^T + \ln P^T - (\ln z_i + \ln \varphi_i + \ln P^z) = 0 \quad (25)$$

The above equation is iteratively solved by an accelerated direct substitution approach based on dominant eigenvalue method, as described by Orbach and Crowe [39]. It should be noticed that, unlike the phase stability test without capillary pressure, the solution of Eq. (25) should take the pressure difference between the trial phase and the feed into consideration, as  $P^T - P^z = \pm P_C$ . The sign before the capillary pressure is positive if the trial phase is the non-wetting (vapor) phase and the feed is the wetting (liquid) phase. The sign is negative if the trial phase and the feed is wetting phase and non-wetting phase respectively.

Based on the solution of the Rachford-Rich equation and the capillary pressure equation, the fugacities, as well as densities of the fluids, are obtained. The algorithm iteratively tunes the solution to minimize the residual of the equilibrium ratio as well as the capillary pressure until certain criteria are satisfied. In this work, the criterion of the convergence of the equilibrium ratio is set as

$$\sum_i \left| \frac{K_i}{K_i^*} - 1 \right| \leq 1.0e^{-4} \quad (26)$$

where  $K_i^*$  is the equilibrium ratio solved at the previous iteration step. A flowchart of the K-value based flash calculation with capillary pressure effect is shown in Fig. 1. The parameters, including binary interaction factor and parachor values, for the physical flash calculation are listed in Appendix A. As an example, the phase envelopes of n-Decane-CO<sub>2</sub> binary mixture with and without the capillary pressure are shown in Fig. 2. Our results match well with experimental results [40].

### 3. Proxy flash calculator

#### 3.1. General information

In this work, we have developed a data-driven flash calculation module based on deep learning techniques to improve the speed and convergence performance of the flash calculation in the unconventional reservoirs. In the new framework, the initial guess of the flash calculation is obtained from a stochastically trained neural network instead of Wilson's equation. We use deep-learning based stochastic training technique to develop the proxy simulator. We have trained a neural network, which has an input layer, an output layer, and four hidden layers. Within each layer, there are several neurons (elements). All neurons belonged to two neighboring layers are fully connected, as shown in Fig. 3.

The neural network adopts fully connected (dense) layers and is trained as a standalone module. Once trained, the neural network predicts the phase condition, capillary pressure as well as concentration

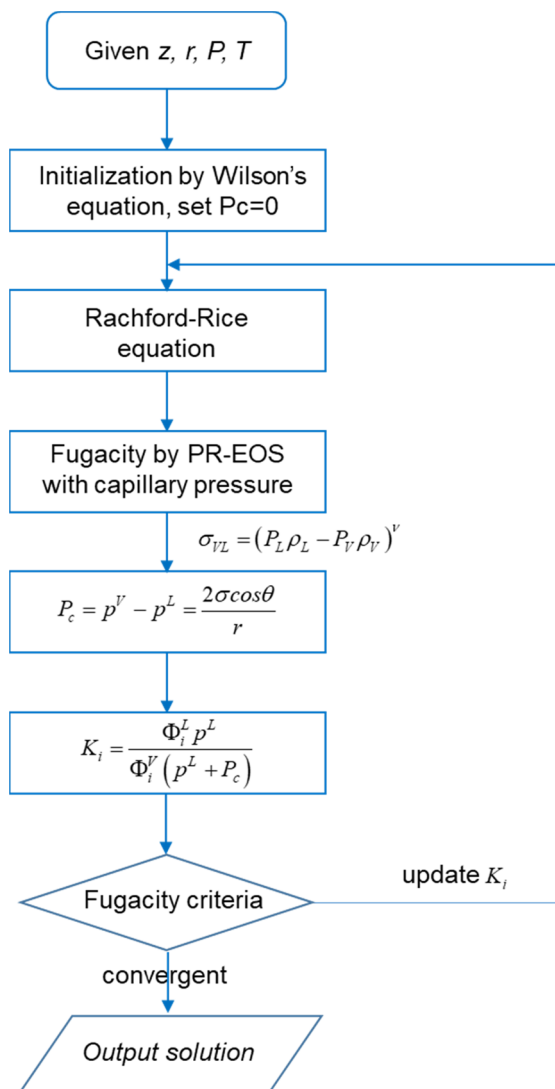


Fig. 1. Flowchart of the K-value based flash calculation with capillary pressure effect.

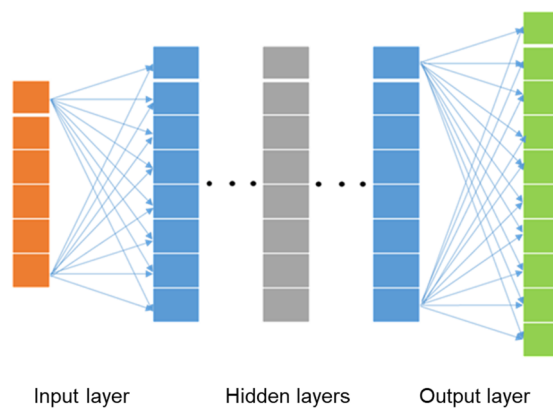


Fig. 3. Conceptual model of the fully connected neural network.

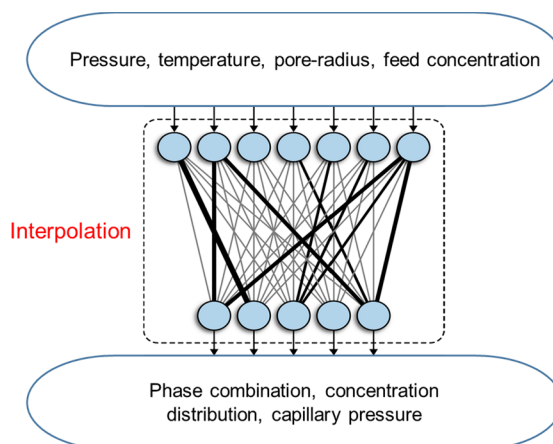


Fig. 4. Conceptual framework of the prediction step.

distribution by simple interpolations. As will be shown in the later chapters, the accuracy of the developed network is above 97%. Therefore, a much more accurate initial guess for the flash calculation can be obtained. The fully connected layers are an imitation of human's neural system. Each element within the network has one weight value and one bias value, indicating the 'contribution' of the element. In the fully connected layers, each element is connected to all elements belonged to its neighboring layers. Activation functions are used between

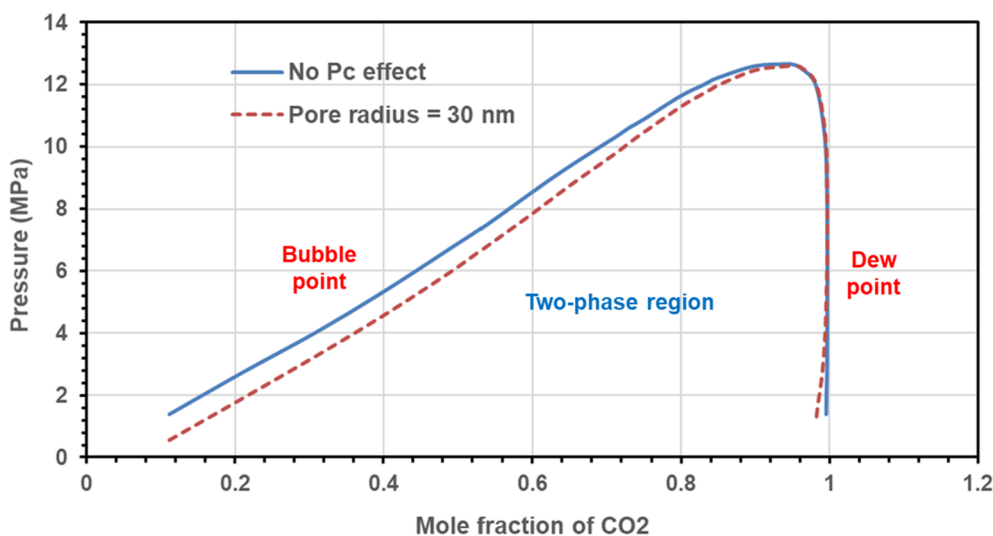


Fig. 2. Phase envelop of n-Decane-CO<sub>2</sub> binary mixture at 71 °C.

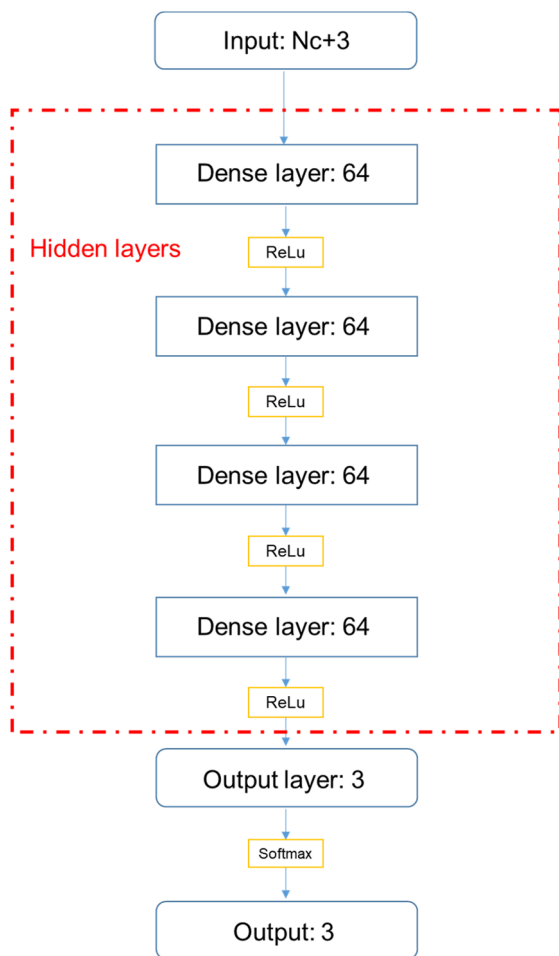


Fig. 5. Structure of the fully connected neural network for the phase classification step. The numbers refer to the dimension of the layers.

layers. For a given set of input parameters, the network predicts the output results by interpolating from the weight values and the bias values. During the training process, the weight and the bias of the elements are optimized by certain optimization algorithms to achieve the best prediction. Then in the prediction step as shown in Fig. 4, the simulator only needs to load the trained weight and bias values into the memory and conduct simple interpolation, which is very cheap in terms of computational time.

In this work, the training process consists of two steps. The first step, which is named the phase classification step, determines the phase condition of the system under the given condition. In the second step, which is named the concentration determination step, the phase ratio, component concentration, and capillary pressure are determined. The input parameters for both steps include pressure, temperature, feed concentration and pore radius. The input parameters are all normalized to [0,1] scale before being substituted into the network.

### 3.2. Phase classification

The network for the phase classification step consists of six layers, including the input layer (layer 1), the output layer (layer 6) and four hidden layers (layer 2–5). The number of input parameters is  $N_c + 3$ . The input parameters  $X$  include the feed concentration, pressure, temperature, and pore radius. All input parameters are normalized to [0,1] scale. The dimension of layer 1 to layer 4 is 64, and the dimension of the output layer is 3. Therefore, the network classifies the phase condition into three types, namely pure vapor phase (V), pure oil phase (L), and double phases (V + L).

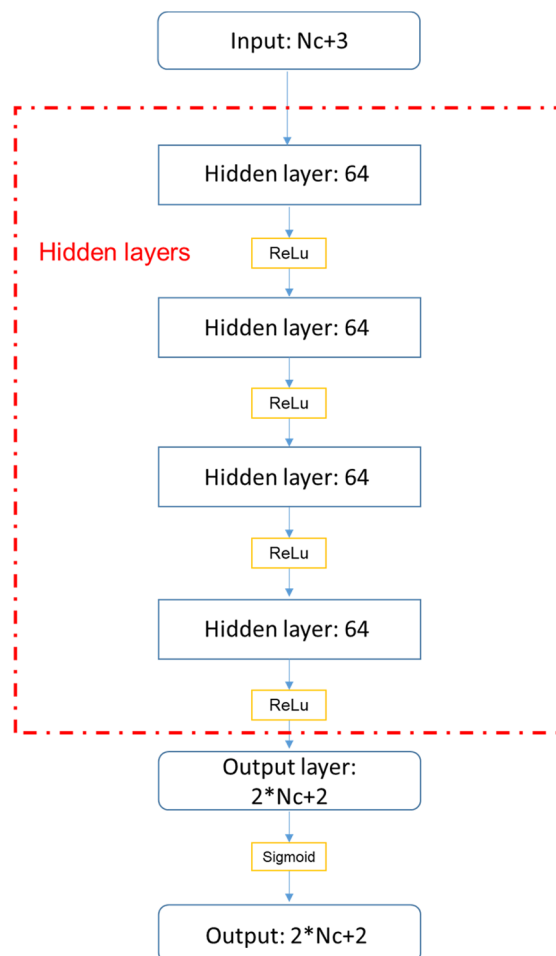


Fig. 6. Structure of the neural network for the concentration determination step. The numbers refer to the dimension of the layers.

Table 1

Range of the parameters of the training samples.

|                    | Unit          | Minimum | Maximum |
|--------------------|---------------|---------|---------|
| Pressure           | MPa           | 1       | 80      |
| Temperature        | °C            | 40      | 100     |
| Pore radius        | nm            | 30      | 100     |
| Feed concentration | dimensionless | 0       | 1       |

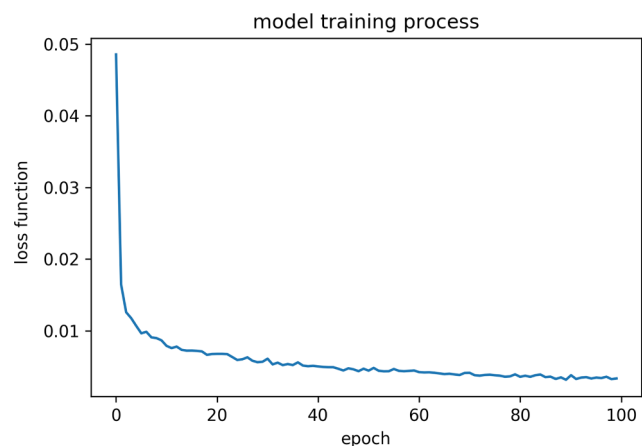
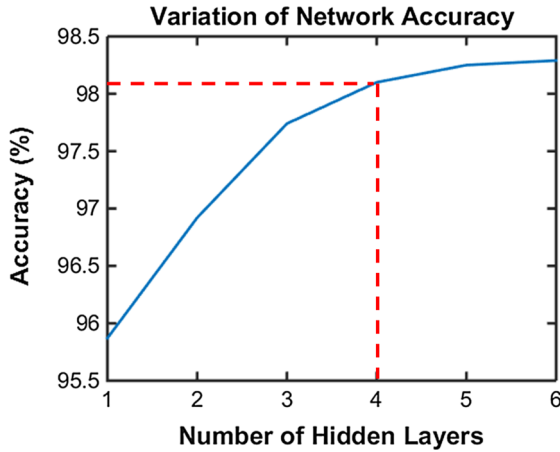


Fig. 7. Variation of the loss function of the phase classification step during the training process of Case 4.

**Table 2**  
Summary of errors of the fully connected network.

| Case index | Feed component                       | Phase Classification<br>Mean Absolute Percentage Error | Concentration Determination<br>Mean Absolute Percentage Error | Overall Accuracy<br>Mean Absolute Percentage Accuracy |
|------------|--------------------------------------|--|---|---|
| 1          | C1 + C2 + C3                         | 0.01%  | 0.46%   | 99.53%  |
| 2          | C1 + C2 + C3 + C6                    | 0.02%  | 0.73%   | 99.25%  |
| 3          | C1 + C2 + C3 + C4 + C5               | 0.02%  | 1.02%   | 98.96%  |
| 4          | C1 + C2 + C3 + C5 + C7 + C9          | 0.04%  | 1.86%   | 98.10%  |
| 5          | C1 + C2 + C3 + C4 + C5 C8 + C9 + C10 | 0.06%  | 2.24%   | 97.83%  |



**Fig. 8.** Comparison of the accuracy with different number of hidden layers for Case 4.

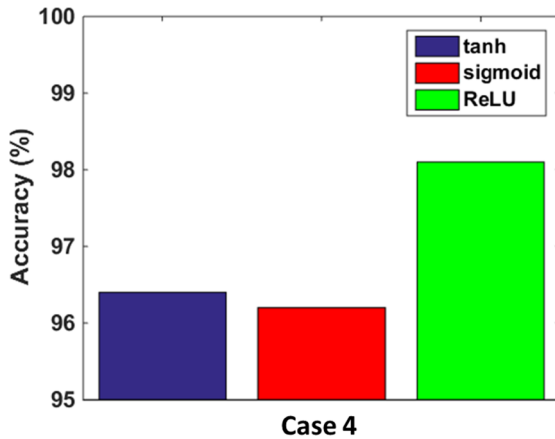


**Fig. 9.** Comparison of the performance of different activation functions for the hidden layers in Case 4.

$$X = [P, T, r, z_1, \dots, z_{N_c}]^T \quad (27)$$

The activation function for layer 1–4 is ReLU function, as follows

$$\text{ReLU}(x) = \begin{cases} 0 & \text{for } x < 0 \\ x & \text{for } x \geq 0 \end{cases} \quad (28)$$

The activation function for the output layer is Softmax function, as follows

$$\text{softmax}(x)_j = \frac{e^{x_j}}{\sum_{k=1}^K e^{x_k}} \quad (29)$$

where  $K$  is the total number of parameters and  $e^x$  is the exponential function. A detailed structure of the network is as shown in Fig. 5.

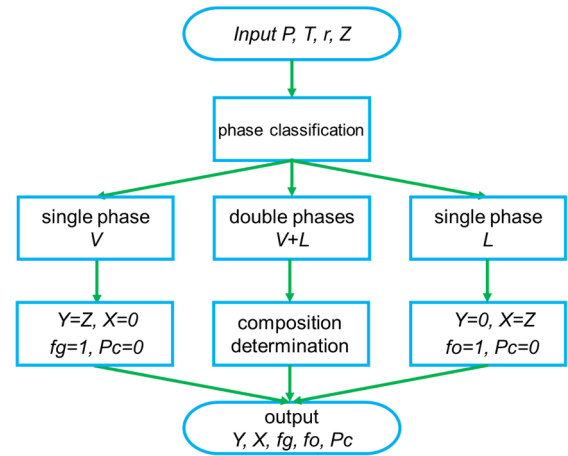


**Fig. 10.** Flowchart of the proxy flash calculation in a reservoir simulator.

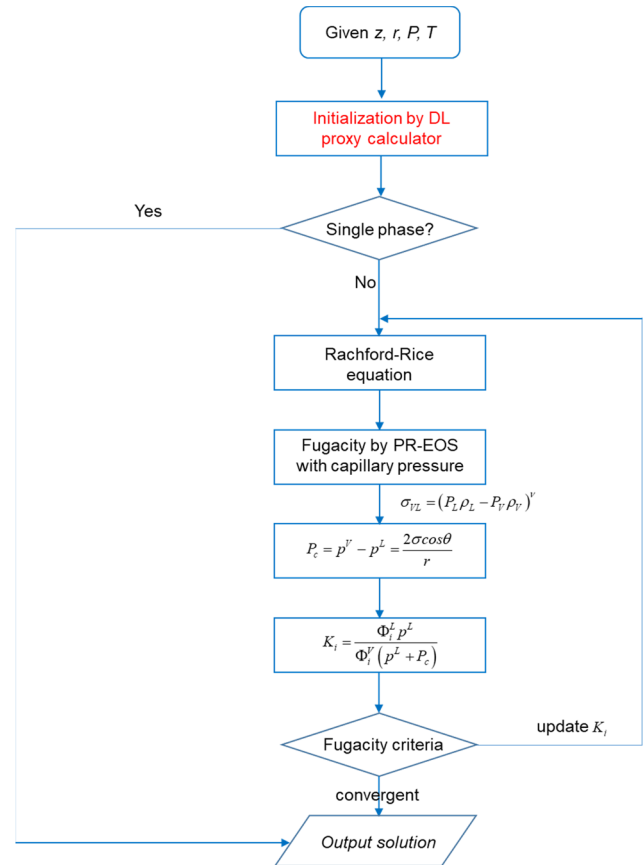


**Fig. 11.** Flowchart of the deep learning based flash calculator.



**Table 3**

Comparison of the number of iterations with and without the number of deep-learning based preconditioner.

| Case index | Feed component                          | Iterations without DL preconditioner | Iterations with DL preconditioner |
|------------|---|--------------------------------------|-----------------------------------|
| 1          | C1 + C2 + C3                            | 3.7                                  | 1.3                               |
| 2          | C1 + C2 + C3 + C6                       | 8.6                                  | 2.0                               |
| 3          | C1 + C2 + C3 + C4 + C5                  | 14.3                                 | 2.2                               |
| 4          | C1 + C2 + C3 + C5 + C7 + C9             | 17.0                                 | 3.6                               |
| 5          | C1 + C2 + C3 + C4 + C5<br>C8 + C9 + C10 | 25.8                                 | 4.5                               |

### 3.3. Concentration determination

The network for the concentration determination step consists of six layers, including the input layer (layer 1), the output layer (layer 6) and four hidden layers (layer 2–5). The dimension, as well as physical meanings of the input parameters of this step, are the same as those of the phase classification step. The dimension of layer 1 to layer 4 is 64, and the dimension of the output layer is  $2N_c + 3$ , including the capillary pressure  $P_c$ , the vapor phase ratio  $n_v$ , the oil phase ratio  $n_L$ , and the component concentration in the vapor phase  $y_i$ ,  $i = 1, \dots, N_c$  and oil phase  $x_i$ ,  $i = 1, \dots, N_c$ . The activation function for layer 1–4 is ReLU function, as shown in Eq. (28). The activation function for the output layer is Sigmoid equation, as shown in Eq. (30).

$$\text{sigmoid}(x) = \frac{1}{1 + e^{-x}} \quad (30)$$

A detailed structure of the network is as shown in Fig. 6.

### 3.4. Training

We have investigated five cases with different combinations of hydrocarbon components. For each case, we use 300,000 training samples generated from the standalone flash calculation module described in Chapter 2. The samples are generated randomly using Latin Hypercube Sampling [41,42] technique. The range of the input parameters is listed in Table 1.

We use stochastic gradient descent (SGD) algorithm [43] to train the network on Keras [44] with a GTX 1080Ti GPU of 11 GB in memory. The algorithm of SGD can be briefly described as follows (Bottou 2012). For an object function  $Q$  with the primary variable  $\mathbf{w}$  of  $n$  dimensions,

$$\Theta(\mathbf{w}) = \frac{1}{n} \sum_{i=1}^n \Theta_i(w_i) \quad (31)$$

Instead of optimizing all  $n$  dimensions at the same time, SGD randomly optimizes a randomly chosen group (batch) of the variables using gradient descent optimization, as below

$$w_{t+1} = w_t - \eta \nabla_j \Theta(w_t) \quad (32)$$

where  $t$  is the number of iteration steps.  $j$  is the index of a batch.  $\eta$  is the learning rate. After the completion of one epoch, all the training samples are shuffled. Hence, the optimization of one high-dimensional problem is effectively converted to the optimization of numerous low-

dimensional problems. In this work, we have compared the choice of the learning rate. The optimal value is found to be 0.001. The neural network for the phase classification step and the concentration determination step is trained with 100 epochs, respectively. We use the mean absolute percentage error (MAPE) as a metric (loss function) during the training, which is defined as follows.

$$\text{MAPE} = \frac{100\%}{N} \sum_{i=1}^N \left| \frac{A_i - F_i}{A_i} \right| \quad (33)$$

In the above equation,  $N$  refers to the number of testing samples.  $A$  and  $F$  refer to actual value and predicted (forecast) value, respectively. The accuracy of the training sample is cross validated by K-folds approach. The training samples are randomly divided into ten groups. For every ten epochs of the training, one group is chosen for testing and the rest of the nine groups are used for training. The variation of the loss function during the training process for Case 5 is shown in Fig. 7. The error metric for each of the five cases is listed in Table 2. According to the results, the accuracy of our neural network is above 97% for the cases we run. We have compared the accuracy of the network with different number of hidden layers and found out network with four hidden layers achieves optimal performance (see Fig. 8). Generally speaking, more hidden layers (with more degree of freedom) result in deeper network and better accuracy. However, beyond a certain level the addition of more layers cannot contribute to accuracy and may even cause over-fitting issue [12]. We have also compared the performance of different activation functions for the hidden layers, including sigmoid function (as defined in Eq. (30)), tanh function [12] and ReLU function (as defined in Eq. (28)) for Case 4. The results are listed in Fig. 9, which shows that ReLU function achieves the highest accuracy. However till today the choice of activation function as well as the number of layers is still like an art. Moreover, as expected when the number of hydrocarbon components increases, the accuracy decreases accordingly, due to the increase of the dimensions in the parameter space. In general, the proxy flash calculator based on deep learning techniques is much more accurate than any other existing techniques.

## 4. Deep learning based flash calculator

The trained deep learning (DL) network is implemented in our flash calculation module. The proxy flash calculator provides the initial guess of the equilibrium ratio as well as the capillary pressure, replacing Wilson's equation. Since the phase classification step is of very high accuracy, the phase condition predicted by that step is adopted as the 'final' result. Therefore, if the phase classification step predicts that only one phase exists in the system, the DL proxy calculator directly outputs the results. If, however, the phase classification step predicts that two phases exist in the system, the flash calculator will start the K-value based iteration using the predicted equilibrium ratio and capillary pressure, until global convergence. A simplified and a detailed flow-chart of the deep learning based flash calculator are shown in Figs. 10 and 11 respectively.

The comparison between the average number of iterations of the flash calculation with and without DL preconditioning is shown in Table 3. According to the comparison of the numerical performance, the number of iterations has been cut by above 50%. According to the

**Table 4**

Comparison of the ratio of convergence with and without the number of deep-learning based preconditioner.

| Case index | Feed component                       | Ratio of convergence without DL preconditioner | Ratio of convergence with DL preconditioner |
|------------|--------------------------------------|--|---|
| 1          | C1 + C2 + C3                         | 96.1%  | 99.4%                                       |
| 2          | C1 + C2 + C3 + C6                    | 94.9%  | 99.1%                                       |
| 3          | C1 + C2 + C3 + C4 + C5               | 93.4%  | 98.8%                                       |
| 4          | C1 + C2 + C3 + C5 + C7 + C9          | 92.7%  | 98.5%                                       |
| 5          | C1 + C2 + C3 + C4 + C5 C8 + C9 + C10 | 91.3%  | 98.3%                                       |

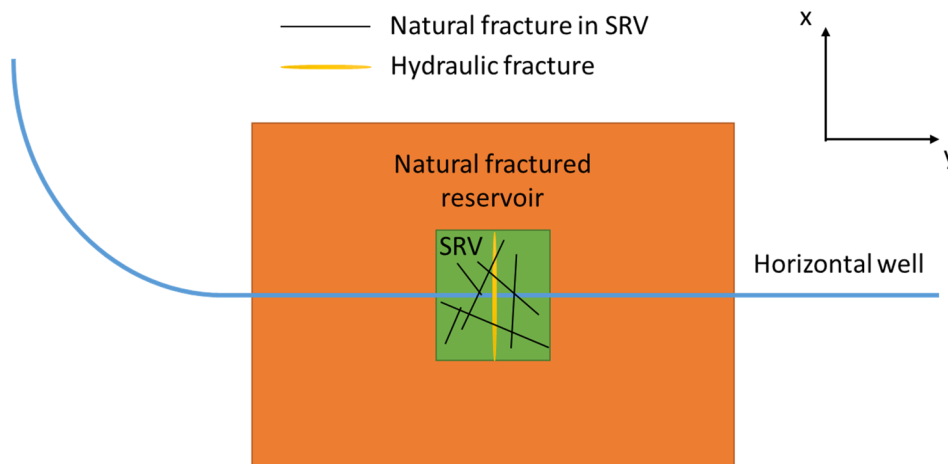


Fig. 12. Conceptual model of the case study with the DL based reservoir simulator.

Table 5

Initial distribution of components for deep learning based compositional reservoir simulation case.

| Component | Formula                        | Mole fraction |
|-----------|--------------------------------|---------------|
| Methane   | CH <sub>4</sub>                | 0.40          |
| Ethane    | C <sub>2</sub> H <sub>6</sub>  | 0.15          |
| Propane   | C <sub>3</sub> H <sub>8</sub>  | 0.15          |
| Butane    | C <sub>4</sub> H <sub>10</sub> | 0.05          |
| n-Pentane | C <sub>5</sub> H <sub>12</sub> | 0.05          |
| n-Heptane | C <sub>7</sub> H <sub>16</sub> | 0.20          |

Table 6

Input parameters for fractured reservoir case.

| Property   | Value | Unit          |
|--|-------|---------------|
| Permeability of the matrix rock                    | 0.1   | μd            |
| Porosity of the matrix rock                        | 0.01  | dimensionless |
| Permeability of the hydraulic fracture             | 100   | md            |
| Porosity of the hydraulic fracture                 | 0.2   | dimensionless |
| Permeability of the fractures in SRV               | 50    | md            |
| Porosity of the fractures in SRV                   | 0.1   | dimensionless |
| Permeability of the fractures outside SRV          | 20    | md            |
| Porosity of the fractures outside SRV              | 0.05  | dimensionless |
| Rock compressibility                               | 0.0   | dimensionless |
| Initial pressure                                   | 21.2  | MPa           |
| Initial temperature                                | 120   | °C            |
| Production pressure                                | 10.2  | MPa           |
| Pore radius  | 50    | nm            |
| Residual gas saturation ( $S_{gr}$ )               | 0.1   | dimensionless |
| Residual oil saturation ( $S_{or}$ )               | 0.1   | dimensionless |
| Maximum gas relative permeability ( $k_{rg,max}$ ) | 0.7   | dimensionless |
| Maximum gas relative permeability ( $k_{ro,max}$ ) | 0.9   | dimensionless |
| $n_g$  | 2.0   | dimensionless |
| $n_o$  | 2.0   | dimensionless |

results, DL based proxy calculation effectively reduces the number of iterations of flash calculation and, thus accelerates the reservoir simulation.

Moreover, we have observed that DL based preconditioner effectively improves the stability (convergence) of flash calculation. The large capillary effect causes the flash calculation with Wilson's initial guess to be difficult to get converged, which prohibits its applications. As shown in Table 4, with the implementation of the DL based preconditioner, the ratio of the converged flash calculations among the 300,000 data sets (parameters shown in Table 1) increases from 90% to above 98%. This is also because that the DL based preconditioner provides a much more accurate initial guess to the flash calculation, making it close enough to the real solution for the Newton-based

algorithm to converge.

## 5. Case study

We have implemented the deep-learning based flash calculator into our simulator MSFLOW\_CO2 and have conducted several case studies to investigate the performance of the deep learning based compositional simulator. In this chapter, all numerical cases are executed by an Intel i7-6700 processor with 3.40 GHz. We have investigated the compositional simulation of a fractured reservoir. The reservoir is naturally fractured. A horizontal well is drilled through the reservoir, and a hydraulic fracture is engineered within the reservoir, creating a stimulated reservoir volume (SRV) in the vicinity of the hydraulic fracture. The conceptual model of the problem is shown in Fig. 12, in which the green and the orange part indicates the area within and outside the SRV, respectively.

The natural fractured reservoir part and the SRV are both modeled as dual-porosity systems. In the dual-porosity system, the fracture network provides flow channel while the matrix rock stores the hydrocarbon. A 'shape-factor' [45–47] is used to quantify the flow between the matrix rock and the fracture network. Wu and Pruess [48] incorporated the shape factor into the integrated finite difference (IFD) framework. Therefore, in this work the single-continuum and dual-porosity model are both discretized using the same IFD approach, as suggested by Wu and Qin [49]. The length of the entire reservoir along x- and y- direction is 540 m and the 400 m, respectively, while the length of the SRV along x- and y-direction is 120 m and 160 m, respectively. The conceptual model of the case is shown in Fig. 12. The relative permeability of the gas phase and the oil phase is modeled by the classic Brooks-Corey model [50], as shown in Eqs. (34) and (35), where  $S_{or}$  and  $S_{gr}$  refers to the residual saturation of the oil and gas phase, respectively.  $k_{ro,max}$  and  $k_{rg,max}$  refer to the maximum relative permeability of the oil and gas phase, respectively.  $n_o$  and  $n_g$  are two constants.

$$k_{ro} = k_{ro,max} \left( \frac{S_o - S_{or}}{1 - S_{or} - S_{gr}} \right)^{n_o} \quad (34)$$

$$k_{rg} = k_{rg,max} \left( \frac{S_g - S_{gr}}{1 - S_{or} - S_{gr}} \right)^{n_g} \quad (35)$$

The initial distribution of components of this case is shown in Table 5. The geomechanical impact is not considered in this case. The input parameters, including the rock properties, are listed in Table 6. We run this case with three different grid block sizes, namely 10 m \* 10 m, 8 m \* 8 m and 4 m \* 4 m for 8 years. As the results, the oil pressure fields of the fracture system and the matrix rock at the end of



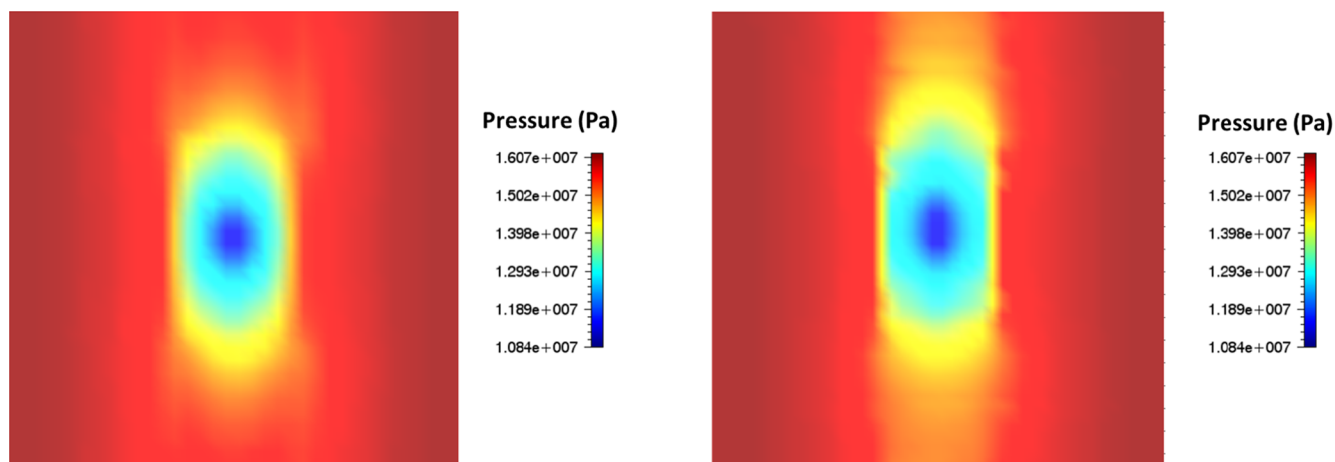


Fig. 13. Comparison of the oil pressure fields of the matrix rock system and the fracture system at the end of the 8-years production. Left: matrix rock system. Right: fracture system.

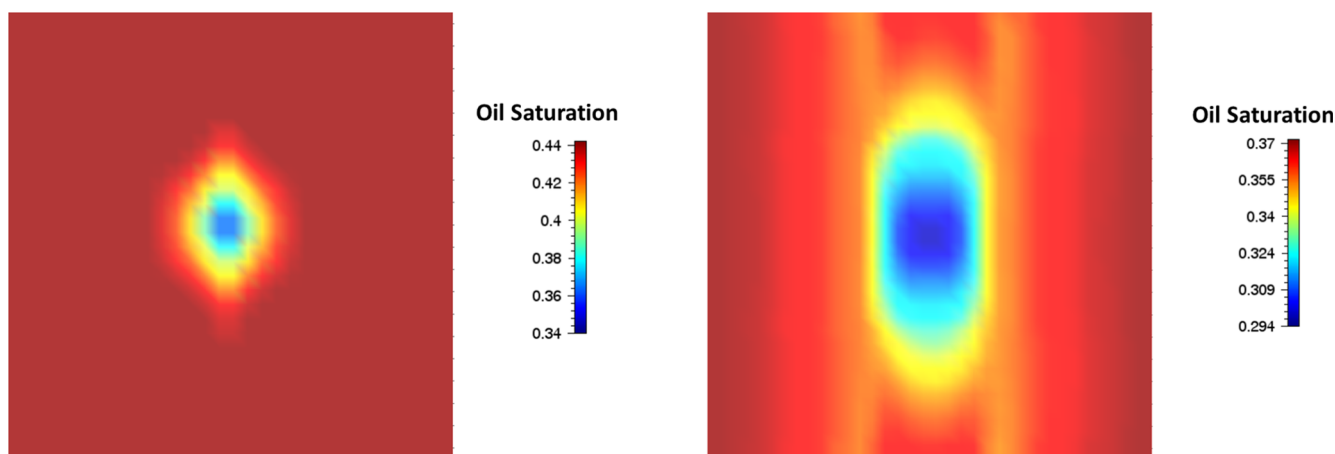


Fig. 14. Comparison of the oil saturation fields of the matrix rock system at the end of the first year of production and at the end of the eighth year of production. Left: end of the first year. Right: end of the eighth year.

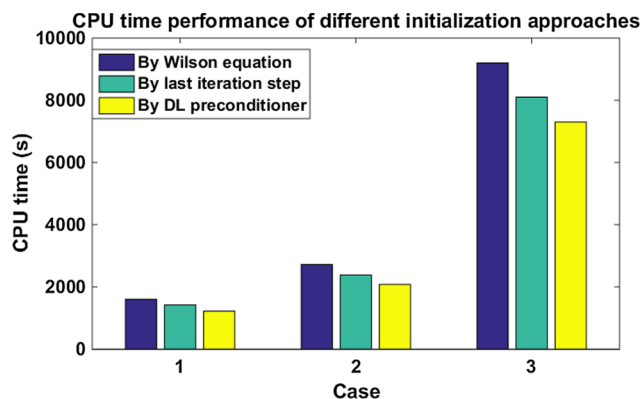


Fig. 15. Comparison of the CPU time of the compositional reservoir simulation cases initialized with different initial guesses.

the production are shown in Fig. 13. The comparison of the oil saturation fields of the matrix rock system at the end of the first year of production and at the end of the eighth year of production is shown in Fig. 14. According to the results, the fractures in the vicinity of the hydraulic fracture get quickly drained by the production, while the pressure inside the matrix rock system declines much slower. As the pressure decreases, the gas phase expands and the oil saturation decreases.

We compare three types of initialization strategy of the flash calculation, namely initializing by Wilson's equation, initializing by the primary variable from the previous NR iteration step, and initializing by the DL preconditioner. In the second type, the initial guess of the equilibrium ratio of the flash calculation is calculated by the primary variable of the last Newton-Raphson iteration step of the same grid block. In the second, the equilibrium ratio is obtained from the deep learning based proxy flash calculation module. The comparison of the CPU time of the three types with different grid block sizes is shown in Fig. 15. According to Fig. 15, the DL preconditioner effectively reduces the CPU time by about 10%–12%, compared to initializing by the equilibrium ratio from the previous iteration step. The results presented in this case show that DL preconditioner is capable of accelerating the performance of large scale compositional simulation for unconventional reservoirs.

## 6. Summary and conclusion

To sum up, we have developed a data-based proxy flash calculator to speed up the time-consuming flash calculation. The proxy flash calculator adopts an initial guess obtained from the deep neural network, the accuracy of which is above 95%. With the implementation of the proxy calculator, the number of iterations of the flash calculation has been effectively reduced by about 50%. Moreover, the stability of the flash calculation has been improved by the DL based preconditioner, with the ratio of convergence increased from 90% to above 98%

percent. This work is among the first trials in this area.

In the present work, the fully-connected neural network is used for the proxy flash calculator. In the future, other structures can also be tried and compared, for instance, the convolutional neural network and the recurrent neural network. Moreover, other portions of the simulator may also be accelerated by the deep learning techniques. For example, the wellbore flow part, which is a very time-consuming simulation of

multiphase flow, can also be replaced by a DL based proxy calculator.

## Acknowledgment

The author would like to thank Energi Simulation for their kind support.

## Appendix A. Parameters for flash calculation

Tables A.1 and A.2.

**Table A.1**

Parameters for the calculation of component properties.

|                                   | Tc (K) | Pc (MPa) | w      | Mw (g·mol <sup>-1</sup> ) | a <sub>0</sub> (KJ·(kg·K) <sup>-1</sup> ) | a <sub>1</sub> (KJ·(kg·K) <sup>-1</sup> ) |
|-----------------------------------|--------|----------|--------|---------------------------|---|---|
| CH <sub>4</sub>                   | 190.56 | 4.599    | 0.0115 | 16.043                    | 2.191                                     | 0.002672                                  |
| C <sub>2</sub> H <sub>6</sub>     | 305.32 | 4.872    | 0.0995 | 30.07                     | 1.651                                     | 0.004384                                  |
| C <sub>3</sub> H <sub>8</sub>     | 369.83 | 4.248    | 0.1523 | 44.096                    | 0.79                                      | 0.00468                                   |
| n-C <sub>4</sub> H <sub>10</sub>  | 408.14 | 3.648    | 0.2002 | 58.123                    | 0.818                                     | 0.004255                                  |
| n-C <sub>5</sub> H <sub>12</sub>  | 469.7  | 3.37     | 0.2515 | 72.15                     | -0.218                                    | 0.001895                                  |
| n-C <sub>6</sub> H <sub>14</sub>  | 507.6  | 3.025    | 0.3013 | 86.177                    | -0.491                                    | 0.007187                                  |
| n-C <sub>7</sub> H <sub>16</sub>  | 540.2  | 2.74     | 0.3495 | 100.204                   | -0.756                                    | 0.007811                                  |
| n-C <sub>8</sub> H <sub>18</sub>  | 568.7  | 2.49     | 0.3996 | 114.231                   | -0.989                                    | 0.00836                                   |
| n-C <sub>9</sub> H <sub>20</sub>  | 594.6  | 2.29     | 0.4435 | 128.258                   | -1.236                                    | 0.008951                                  |
| n-C <sub>10</sub> H <sub>22</sub> | 617.7  | 2.11     | 0.4923 | 142.285                   | -1.465                                    | 0.009484                                  |
| CO <sub>2</sub>                   | 304.3  | 7.39     | 0.2236 | 44.01                     | 0.727                                     | 0.003722                                  |

**Table A.2**

Parachor values for all hydrocarbon components.

| Component                         | Parachor |
|-----------------------------------|----------|
| CH <sub>4</sub>                   | 77.0     |
| C <sub>2</sub> H <sub>6</sub>     | 108.0    |
| C <sub>3</sub> H <sub>8</sub>     | 150.3    |
| n-C <sub>4</sub> H <sub>10</sub>  | 203.4    |
| n-C <sub>5</sub> H <sub>12</sub>  | 231.5    |
| n-C <sub>6</sub> H <sub>14</sub>  | 271.0    |
| n-C <sub>7</sub> H <sub>16</sub>  | 312.5    |
| n-C <sub>8</sub> H <sub>18</sub>  | 351.5    |
| n-C <sub>9</sub> H <sub>20</sub>  | 393.0    |
| n-C <sub>10</sub> H <sub>22</sub> | 617.7    |

## Appendix B. Supplementary data

Supplementary data to this article can be found online at <https://doi.org/10.1016/j.fuel.2019.05.023>.

## References

- [1] Jin B, Nasrabadi H. Phase behavior of multi-component hydrocarbon systems in nano-pores using gauge-GCMC molecular simulation. *Fluid Phase Equilib* 2016;425:324–34. <https://doi.org/10.1016/J.FLUID.2016.06.018>.
- [2] Travalloni L, Castier M, Tavares FW. Phase equilibrium of fluids confined in porous media from an extended Peng-Robinson equation of state. *Fluid Phase Equilib* 2014;362:335–41. <https://doi.org/10.1016/J.FLUID.2013.10.049>.
- [3] Xiong Y. Development of a compositional model fully coupled with geomechanics and its application to tight oil reservoir simulation. Colorado School of Mines. Arthur Lakes Library; 2015.
- [4] Zhang Y, Lashgari HR, Di Y, Sepehrnoori K. Capillary pressure effect on hydrocarbon phase behavior in unconventional reservoirs. *SPE Low Perm Symp.*. Society of Petroleum Engineers; 2016. doi:10.2118/180235-MS.
- [5] Wang S, Pomerantz AE, Xu W, Lukyanov A, Kleinberg RL, Wu Y-S. The impact of kerogen properties on shale gas production: a reservoir simulation sensitivity analysis. *J Nat Gas Sci Eng* 2017;48. <https://doi.org/10.1016/j.jngse.2017.06.009>.
- [6] Kuila U, Prasad M. Understanding pore-structure and permeability in shales. *SPE Annu. Tech. Conf. Exhib.*. Society of Petroleum Engineers; 2011. doi:10.2118/146869-MS.
- [7] Wang S, Lukyanov AA, Wang L, Wu Y-S, Pomerantz A, Xu W, et al. A non-empirical gas slippage model for low to moderate Knudsen numbers. *Phys Fluids* 2017;29. <https://doi.org/10.1063/1.4974319>.
- [8] Wang S, Pan Z, Zhang J, Yang Z, Wang Y, Wu Y-S, et al. On the Klinkenberg effect of multicomponent gases. *Proc – SPE Annu Tech Conf Exhib* 2017.
- [9] Wang S, Lukyanov AA, Wu Y-S. Second-order gas slippage model for the Klinkenberg effect of multicomponent gas at finite Knudsen numbers up to 1. *Fuel* 2019;235:1275–86. <https://doi.org/10.1016/J.FUEL.2018.08.113>.
- [10] Okuno R, Johns R, Sepehrnoori K. A new algorithm for rachford-rice for multiphase compositional simulation. *SPE J* 2010;15:313–25. <https://doi.org/10.2118/117752-PA>.
- [11] Nichita DV, Gomez S, Luna E. Multiphase equilibria calculation by direct minimization of Gibbs free energy with a global optimization method. *Comput Chem Eng* 2002;26:1703–24. [https://doi.org/10.1016/S0098-1354\(02\)00144-8](https://doi.org/10.1016/S0098-1354(02)00144-8).
- [12] LeCun Y, Bengio Y, Hinton G. Deep learning. *Nature* 2015;521:436–44. <https://doi.org/10.1038/nature14539>.
- [13] Gaganis V, Varotsis N. Machine learning methods to speed up compositional reservoir simulation. *SPE Eur. Annu. Conf.*. Society of Petroleum Engineers; 2012. doi:10.2118/154505-MS.

- [14] Gaganis V, Varotsis N. An integrated approach for rapid phase behavior calculations in compositional modeling. *J Pet Sci Eng* 2014;118:74–87. <https://doi.org/10.1016/J.PETROL.2014.03.011>.
- [15] Kashinath A, Szulczewski ML, Dogru AH. A fast algorithm for calculating isothermal phase behavior using machine learning. *Fluid Phase Equilib* 2018;465:73–82. <https://doi.org/10.1016/J.FLUID.2018.02.004>.
- [16] Tipping EM. The relevance vector machine. 12th Int. Conf. Neural Inf. Process. Syst. Denver, CO: MIT Press; 1999. p. 652–8.
- [17] El-Sebakhy EA. Forecasting PVT properties of crude oil systems based on support vector machines modeling scheme. *J Pet Sci Eng* 2009;64:25–34. <https://doi.org/10.1016/J.PETROL.2008.12.006>.
- [18] Rafiee-Taghanaki S, Arabloo M, Chamkalani A, Amani M, Zargari MH, Adelzadeh MR. Implementation of SVM framework to estimate PVT properties of reservoir oil. *Fluid Phase Equilib* 2013;346:25–32. <https://doi.org/10.1016/J.FLUID.2013.02.012>.
- [19] Burges CJC. A tutorial on support vector machines for pattern recognition. *Data Min Knowl Discov* 1998;2:121–67. <https://doi.org/10.1023/A:1009715923555>.
- [20] Kobayashi K, Komaki F. Information criteria for support vector machines. *IEEE Trans Neural Networks* 2006;17:571–7. <https://doi.org/10.1109/TNN.2006.873276>.
- [21] Schölkopf B, Smola AJ. *Learning with kernels : support vector machines, regularization, optimization, and beyond*. first ed. MIT Press; 2002.
- [22] Vapnik V. *The nature of statistical learning theory*. second ed. New York: Springer; 2000.
- [23] Gharbi RB, Elsharkawy Adel M, Karkoub M. Universal neural-network-based model for estimating the PVT properties of crude oil systems. *Energy Fuel* 1999. <https://doi.org/10.1021/EF980143V>.
- [24] Kamyab M, Sampaio JH, Qanbari F, Eustes AW. Using artificial neural networks to estimate the z-factor for natural hydrocarbon gases. *J Pet Sci Eng* 2010;73:248–57. <https://doi.org/10.1016/J.PETROL.2010.07.006>.
- [25] Nikravesh M, Aminzadeh F, Zadeh LA. *Soft computing and intelligent data analysis in oil exploration*. Elsevier; 2003.
- [26] Wang S. *Numerical study of thermal-hydraulic-mechanical behavior of fractured geothermal reservoirs*. Colorado School of Mines; 2015.
- [27] Wu Y. MSFLOW: multiphase subsurface flow model of oil. gas and water in porous and fractured media with water shutoff capability, documentation and user's guide. Walnut Creek, California; 1998.
- [28] Narasimhan TN, Witherspoon PA. An integrated finite difference method for analyzing fluid flow in porous media. *Water Resour Res* 1976;12:57–64. <https://doi.org/10.1029/WR012i001p00057>.
- [29] Larsbo M, Roullet S, Stenemo F, Kasteel R, Jarvis N. An improved dual-permeability model of water flow and solute transport in the Vadose Zone. *Vadose Zone J* 2005;4:398. <https://doi.org/10.2136/vzj2004.0137>.
- [30] Wang S, Lukyanov AA, Wu Yu-Shu. Application of algebraic smoothing aggregation two level preconditioner to multiphysics fluid flow simulations in porous media. Galveston, Texas: SPE Reserv. Simul. Conf.; 2019.
- [31] Wang L, Wang S, Zhang R, Wang C, Xiong Y, Zheng X, et al. Review of multi-scale and multi-physical simulation technologies for shale and tight gas reservoirs. *J Nat Gas Sci Eng* 2017;37:560–78. <https://doi.org/10.1016/j.jngse.2016.11.051>.
- [32] Wang L, Tian Y, Yu X, Wang C, Yao B, Wang S, et al. Advances in improved/enhanced oil recovery technologies for tight and shale reservoirs. *Fuel* 2017;210:425–45. <https://doi.org/10.1016/J.FUEL.2017.08.095>.
- [33] Macleod DB. On a relation between surface tension and density. *Trans Faraday Soc* 1923;19:38. <https://doi.org/10.1039/tf9231900038>.
- [34] Sugden S. VI.—The variation of surface tension with temperature and some related functions. *J Chem Soc Trans* 1924;125:32–41. <https://doi.org/10.1039/CT9242500032>.
- [35] Sherafati M, Jessen K. Stability analysis for multicomponent mixtures including capillary pressure. *Fluid Phase Equilib* 2017;433:56–66. <https://doi.org/10.1016/J.FLUID.2016.11.013>.
- [36] Peng D-Y, Robinson DB. A new two-constant equation of state. *Ind Eng Chem Fundam* 1972;51:385–1082.
- [37] Lemmon WE. NIST Reference Fluid Thermodynamic and Transport Properties-REFPROP, Ver. 7.0. NIST Stand Ref Database 2002.
- [38] Michelsen ML. The isothermal flash problem. Part I. Stability. *Fluid Phase Equilib* 1982;9:1–19. [https://doi.org/10.1016/0378-3812\(82\)85001-2](https://doi.org/10.1016/0378-3812(82)85001-2).
- [39] Orbach O, Crowe CM. Convergence promotion in the simulation of chemical processes with recycle-the dominant eigenvalue method. *Can J Chem Eng* 1971;49:509–13. <https://doi.org/10.1002/cjce.5450490414>.
- [40] Reamer HH, Sage BH. Phase equilibria in hydrocarbon systems. Volumetric and phase behavior of the n-Decane-CO<sub>2</sub> system. *J Chem Eng Data* 1963;8:508–13. <https://doi.org/10.1021/je60019a010>.
- [41] Iman RL, Iman LR. Latin hypercube sampling. *Encycl. Quant. Risk Anal. Assess.. Chichester, UK: John Wiley & Sons, Ltd; 2008*. doi:10.1002/9780470061596.risk0299.
- [42] Stein M. Large sample properties of simulations using latin hypercube sampling. *Technometrics* 1987;29:143–51. <https://doi.org/10.1080/00401706.1987.10488205>.
- [43] Bottou L. Large-scale machine learning with stochastic gradient descent. In: *Proc. COMPSTAT'2010*, Heidelberg: Physica-Verlag HD; 2010, p. 177–86. doi:10.1007/978-3-7908-2604-3\_16.
- [44] Chollet F. Keras. 2015.
- [45] Warren JE, Root PJ. The behavior of naturally fractured reservoirs. *Soc Pet Eng J* 1963;3:245–55. <https://doi.org/10.2118/426-PA>.
- [46] Gilman JR, Kazemi H. Improvements in simulation of naturally fractured reservoirs. *Soc Pet Eng J* 1983;23:695–707. <https://doi.org/10.2118/10511-PA>.
- [47] Lim KT, Aziz K. Matrix-fracture transfer shape factors for dual-porosity simulators. *J Pet Sci Eng* 1995;13:169–78. [https://doi.org/10.1016/0920-4105\(95\)00010-F](https://doi.org/10.1016/0920-4105(95)00010-F).
- [48] Wu Y-S, Pruess K. A multiple-porosity method for simulation of naturally fractured petroleum reservoirs. *SPE Reserv Eng* 1988;3:327–36. <https://doi.org/10.2118/15129-PA>.
- [49] Wu Y-S, Qin G. A generalized numerical approach for modeling multiphase flow and transport in fractured porous media. *Commun Comput Phys* 2009;6:85–108.
- [50] Delshad M, Pope G. Comparison of the three-phase oil relative permeability models. *Transp Porous Media* 1989;4:59–83. <https://doi.org/10.1007/BF00134742>.